Title

Femtosecond time-resolved XUV + UV photoelectron imaging of pure helium nanodroplets.

Journal

The Journal of chemical physics, 141(17)

ISSN

0021-9606

Authors

Ziemkiewicz, Michael P
Bacellar, Camila
Siefermann, Katrin R
et al.

Publication Date

2014-11-01

DOI

10.1063/1.4900503

Peer reviewed

AIP | The Journal of Chemical Physics

Femtosecond time-resolved XUV + UV photoelectron imaging of pure helium nanodroplets

Michael P. Ziemkiewicz, Camila Bacellar, Katrin R. Siefermann, Stephen R. Leone, Daniel M. Neumark, and Oliver Gessner

Citation: The Journal of Chemical Physics **141**, 174306 (2014); doi: 10.1063/1.4900503
View online: http://dx.doi.org/10.1063/1.4900503
View Table of Contents: http://scitation.aip.org/content/aip/journal/jcp/141/17?ver=pdfcov
Published by the AIP Publishing

Femtosecond time-resolved XUV + UV photoelectron imaging of pure helium nanodroplets

Michael P. Ziemkiewicz,[1,2] Camila Bacellar,[1,2] Katrin R. Siefermann,[1,2]
Stephen R. Leone,[1,2,3] Daniel M. Neumark,[1,2] and Oliver Gessner[1]
[1]*Ultrafast X-ray Science Laboratory, Chemical Sciences Division, Lawrence Berkeley National Laboratory, Berkeley, California 94720, USA*
[2]*Department of Chemistry, University of California, Berkeley, California 94720, USA*
[3]*Department of Physics, University of California, Berkeley, California 94720, USA*

(Received 30 August 2014; accepted 15 October 2014; published online 4 November 2014)

Liquid helium nanodroplets, consisting of on average 2×10^6 atoms, are examined using femtosecond time-resolved photoelectron imaging. The droplets are excited by an extreme ultraviolet light pulse centered at 23.7 eV photon energy, leading to states within a band that is associated with the 1*s*3*p* and 1*s*4*p* Rydberg levels of free helium atoms. The initially excited states and subsequent relaxation dynamics are probed by photoionizing transient species with a 3.2 eV pulse and using velocity map imaging to measure time-dependent photoelectron kinetic energy distributions. Significant differences are seen compared to previous studies with a lower energy (1.6 eV) probe pulse. Three distinct time-dependent signals are analyzed by global fitting. A broad intense signal, centered at an electron kinetic energy (eKE) of 2.3 eV, grows in faster than the experimental time resolution and decays in ∼100 fs. This feature is attributed to the initially excited droplet state. A second broad transient feature, with eKE ranging from 0.5 to 4 eV, appears at a rate similar to the decay of the initially excited state and is attributed to rapid atomic reconfiguration resulting in Franck-Condon overlap with a broader range of cation geometries, possibly involving formation of a Rydberg-excited $(He_n)^*$ core within the droplet. An additional relaxation pathway leads to another short-lived feature with vertical binding energies $\gtrsim$2.4 eV, which is identified as a transient population within the lower-lying 1*s*2*p* Rydberg band. Ionization at 3.2 eV shows an enhanced contribution from electronically excited droplet states compared to ejected Rydberg atoms, which dominate at 1.6 eV. This is possibly the result of increased photoelectron generation from the bulk of the droplet by the more energetic probe photons. © *2014 AIP Publishing LLC*. [http://dx.doi.org/10.1063/1.4900503]

I. INTRODUCTION

Helium nanodroplets provide a fascinating opportunity for studying spectroscopy and chemistry in an ultracold environment. These superfluid nanostructures consist of $\sim 10^3$–10^9 atoms and evaporatively cool to very low temperatures (∼0.37 K) due to the extremely small He-He binding energy in the liquid phase (∼0.6 meV).[1–4] Their ability to trap molecules at low temperature opens a new regime for studies in spectroscopy, cluster formation, and chemical bonding.[4–11] The sizes and shapes of He droplets have been characterized by x-ray and electron diffraction,[12,13] and large rotating He droplets doped with Xe atoms have recently been shown to support lattices of quantum vortices.[13]

The dynamics of electronically excited He droplet states are of considerable interest since they provide benchmarks for our understanding of complex electronic structures and coupling mechanisms that emerge from the superposition of atomic Rydberg manifolds in nanometer- to micrometer-scale systems.[14–16] For example, droplet electronic excitation leads to various relaxation channels including Penning ionization of embedded species, ejection of Rydberg atoms, and autoionization.[17–23] The present study uses time-resolved photoelectron spectroscopy[24,25] to observe relaxation dynamics in pure helium nanodroplets following extreme ultraviolet (XUV) excitation, with a higher probe photon energy than in our previously reported experiments.[20,21,26,27] It reveals dynamics attributed to the formation of a molecular He_n^* Rydberg core within the droplet and interband decay from the initially excited 1*s*3*p*,4*p* Rydberg band to the lower-lying 1*s*2*p* band.

The electronically excited states of pure He droplets can only be accessed by photon energies in excess of 20.8 eV.[28] The electronic structure and dynamics of these species have been studied using electron impact, synchrotron radiation, high harmonic generation (HHG) based light sources, and free electron lasers (FEL's).[17,18,22,23,26,29–34] Joppien *et al.*[28] performed an XUV fluorescence yield study and identified two strong electronic excitation features below the atomic ionization threshold. The lower lying band is centered at 21.6 eV and appears to be derived from the nearby 1*s*2*p* (^{1}P) level of free atomic helium. There is also a higher energy band centered at 23.9 eV, which is blue-shifted by 0.8 eV relative to the 1*s*3*p* (^{1}P) atomic level and is associated with Rydberg excitations predominantly comprising perturbed 1*s*3*p* and 1*s*4*p* atomic states.[28,35] The ionization potential (IP) of He droplets is ∼23.0 eV, substantially lower than the IP of isolated helium atoms (24.59 eV).[17,18,36] Synchrotron based photoionization experiments also found that excitation of the higher-lying droplet band results in the production of electrons with

near-zero kinetic energy (ZEKE), a process attributed to autoionization. Synchrotron experiments on pure droplets at photon energies well above the IP of helium yielded a vertical IP of 24.5 eV, slightly lower than that of atomic He.[31]

In order to understand the relaxation dynamics that take place in these excited states, our group has carried out a series of experiments based on time-resolved photoelectron and photoion imaging.[20,21,26,27] Owing to the relatively low probe photon energy, 1.6 eV, these experiments were insensitive to electron dynamics occurring in levels bound by more than this energy with respect to ionization. For this reason, we have chosen to perform a new set of pump-probe photoelectron imaging experiments using a 3.2 eV (388 nm) probe pulse, which allows access to deeper levels of electronically excited droplets.

In the new studies, photoelectrons generated at short time delays are emitted with kinetic energies characteristic of the same initially excited droplet state seen in the 1.6 eV probe pulse experiments. As this population decays, a broad photoelectron feature appears, notably extending to higher electron kinetic energy (eKE). This feature is consistent with relaxation channels that produce molecular Rydberg-excited He_n^* cores within the droplet, which exhibit improved Franck-Condon overlap with covalently bound He_n^+ cationic cluster geometries. A second decay channel is also observed, resulting in a new feature at considerably lower kinetic energies. This channel is attributed to interband relaxation to the $1s2p$ Rydberg manifold, which was out of range in previous studies at 1.6 eV. Comparison of results with the two probe colors shows more contributions from photoionization of the electronically excited droplets and less signal from ejected Rydberg atoms at 3.2 eV, suggesting a more pronounced bulk sensitivity compared to the 1.6 eV probe measurements.

II. EXPERIMENT

The experimental setup is shown in Figure 1. Helium nanodroplets are formed using a cryogenically cooled continuous free jet. Electronic dynamics are initiated by an XUV pump pulse at a photon energy of 23.7 eV followed by a 3.2 eV (or 1.6 eV) probe pulse. Photoelectrons are detected using a velocity map imaging (VMI) spectrometer. The basic setup has been discussed in previous publications,[20,26,30] so only a brief overview will be given here, with special emphasis on changes made to the probe beam path in order to use ultraviolet (UV) light.

In the droplet source,[30] 99.9999% pure He at 80 bars is expanded into a 7×10^{-2} Pa vacuum through a 5 μm nozzle cooled to 13 K resulting in an average of 2×10^6 atoms/droplet.[3] Initial electronic excitation is accomplished using 23.7 eV photons produced by femtosecond high harmonic generation (HHG). Infrared light is removed from the beam using a pair of silicon Brewster mirrors and a 200 nm thick tin foil, which also strongly suppresses any XUV light beyond 24 eV. The pump pulse provides $5(1) \times 10^5$ photons/pulse in the 15th harmonic with a photon energy spectrum that peaks at 23.7 eV and has a full width at half maximum (FWHM) of 0.5 eV, as determined by photoelectron spectroscopy of atomic argon. The probe pulse is produced

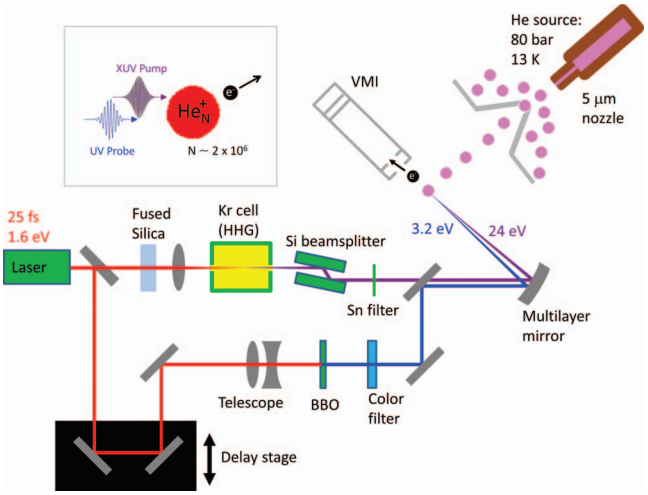

FIG. 1. Experimental setup: Nanodroplets are formed by expanding 80 bars of 99.9999% purity He through a 5 μm hole at 13 K. They are electronically excited at 23.7 eV before being photoionized at 3.2 eV. Both pulses originate from a ~ 25 fs, 3.3 mJ, 775 nm pulse produced by a titanium sapphire laser. The 23.7 eV photons are created by high harmonic generation in a krypton filled gas cell. The 3.2 eV photons are produced by doubling the 1.6 eV IR beam in a BBO crystal. Photoelectron momentum distributions are measured by velocity map imaging.

by splitting off 15% of the 1.6 eV fundamental beam for second harmonic generation in a 500 μm thick BBO crystal. The 3.2 eV beam is filtered by two mirrors coated to reflect the doubled light and to transmit the IR fundamental. It then passes through a BG 40 (Schott) color filter, which rejects the remaining IR.

The peak probe intensity in the interaction region is estimated to be $\sim 8 \times 10^{11}$ W/cm^2, which is expected to be within a regime free of multiphoton effects. Photoelectron momentum distributions are measured using a three plate VMI spectrometer as described previously.[26,37] The temporal instrument response function of the apparatus was measured by pump-probe ionization of atomic helium excited to the $1s4p$ state by the pump laser, yielding a cross-correlation of 123(16) fs (FWHM).

III. RESULTS

Figure 2 shows characteristic electron momentum images taken over a range of pump-probe time delays using 3.2 eV (top row) and 1.6 eV (bottom row) probe pulses. The latter are similar to previously published work.[20] The originally recorded photoelectron velocity-map images have been transformed to the displayed two-dimensional momentum images using a BASEX algorithm.[24] Delays are labeled as positive when the XUV pump pulse precedes the near-IR/UV probe. At negative delays, the results at both wavelengths are identical to those obtained with the pump pulse only. At 3.2 eV, starting at time zero (when pump and probe are overlapped in time), an isotropic ring appears, broadens, and then decreases nearly back to the background level within several hundred fs. At 1.6 eV, an isotropic ring is also observed at short delays and is smaller than at 3.2 eV, consistent with the lower probe photon energy. At the same time, a highly anisotropic channel

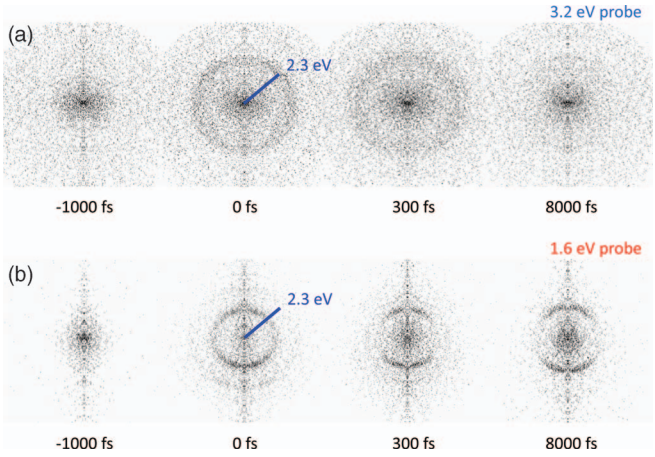

FIG. 2. Photoelectron velocity map images (after BASEX transformation) using (a) a 3.2 eV ultraviolet (UV) probe and (b) a 1.6 eV infrared (IR) probe. The IR results show a more anisotropic character, indicating a higher relative sensitivity to isolated Rydberg atoms ejected from the droplet. The UV probe produces two main rings, a higher energy one that grows in quickly and decays on the timescale of hundreds of femtoseconds and a lower energy one that arrives more slowly before also decaying away. The blue line indicates the radius corresponding to an electron kinetic energy of 2.3 eV.

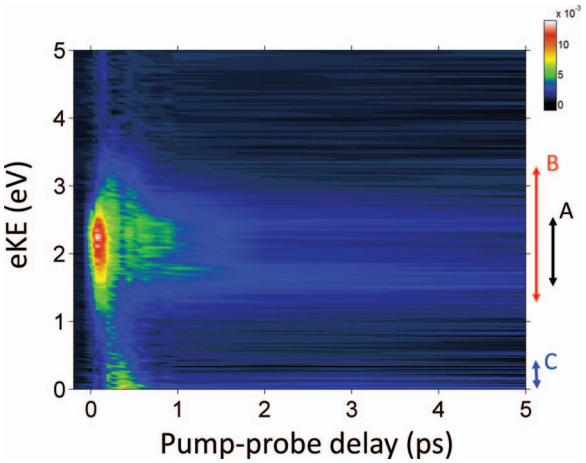

FIG. 3. Photoelectron signal versus electron kinetic energy (eKE) and pump-probe time delay. Positive delay values correspond to the XUV pulse coming first. The initial feature A quickly transitions to a broader feature B, which extends both to higher and lower eKE. As these populations decay, a more deeply bound level C grows in. This feature is likely due to interband relaxation from the $1s3p,4p$ droplet band down to the $1s2p$ band.

appears within the instrument response time and then retains constant intensity for the remainder of the 8 ps delay range spanned by this experiment.[20,26] While this feature dominates the 1.6 eV spectra by 300 fs, it is largely absent from the images at 3.2 eV.

Additionally, for each probe frequency, a narrow but intense feature is seen at the center of the distribution.[18] It arises from ZEKE electrons that can be produced by the pump laser alone as evidenced by their existence at negative time delays. This well-known indirect ionization channel occurs for XUV photon energies above 23 eV, and its eKE distribution, ranging from about 0–10 meV, is independent of the pump energy.[18] The ZEKE signal in this experiment is largely insensitive to pump-probe delay at 3.2 eV. As a result, it is mostly removed when the pump-only background is subtracted, as is done for all further analysis below. Note that the ZEKE signal exhibits a more noticeable time-dependence when probing at 1.6 eV,[20] a result discussed in Sec. V.

Figure 3 shows the evolution of background-subtracted photoelectron kinetic energy spectra as a function of pump-probe time delay. Three main channels are observed and labeled A, B, and C in order of temporal arrival. Channel A appears first and is the most intense. At its peak ($\Delta t = 100$ fs), it spans from 1.7 eV to 3.2 eV half-maximum to half-maximum. As A decays, a new feature (C) appears at lower energies (0.01 to 0.8 eV) before it too decays. Note that the lower limit of this energy range is chosen in order to suppress contributions from the ZEKE channel in the subsequent analysis. A third transient (feature B) is characterized by energies that spread above and below those associated with the initially excited state A. In fact, some electron kinetic energies in this channel exceed $h\nu_{probe}$ (3.2 eV), a sub-population we refer to as superenergetic.

Figure 4 shows photoelectron kinetic energy distributions at three time delays. The black line, taken at $\Delta t = 10$ fs, shows the eKE spectrum of feature A. It peaks at 2.3 eV and has an asymmetric lineshape characterized by half-widths of 0.2 eV and 0.5 eV towards the high and low energy sides, respectively (measured at half maximum relative to 2.3 eV). The blue line shows the eKE distribution at $\Delta t = 360$ fs, well after the peak of feature A. Note that the overall intensities of the three traces in Figure 4 are not scaled with respect to each other and instead represent the actual absolute intensity distributions at different delays. Therefore, the blue curve clearly shows the delayed growth of both the superenergetic component of feature B and the low energy feature C at the expense of feature A. The red curve shows the eKE distribution at $\Delta t = 3$ ps, where feature C has effectively disappeared but a significant population remains in the range spanned by the overlapping features A and B. The dashed curves represent the results of a global least-squares fit as described in Sec. IV.

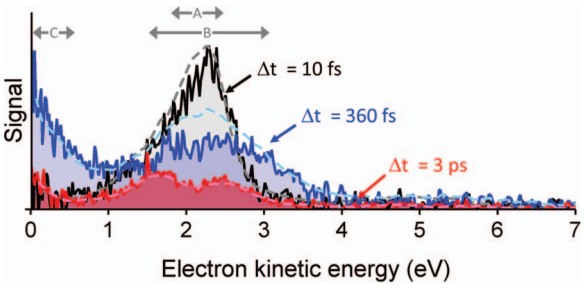

FIG. 4. Kinetic energy distributions at several pump-probe time delays. At early times, the distribution is characterized by a broad feature (A) centered at 2.3 eV, which corresponds to ionization from the initially excited electronic manifold. As this feature decays away, two new ones appear, one containing photoelectrons with larger eKE than in the initially excited state (feature B), and one with a maximum at 0 eV (feature C). Note that the initially excited state reaches its maximum intensity at a time delay of approximately 70 fs, at which point its peak signal is twice as high as in the 10 fs trace shown here. Dashed lines show the results of a global least-squares fit, which is discussed in detail in Sec. IV.

IV. ANALYSIS

Our data consist of three transient dynamical features, all of which overlap to some extent in the energy domain but exhibit significantly different behavior in the time domain. For this reason, the data are analyzed using a global fitting procedure[27,38] in which spectral distributions are extracted based on the assumption of separable dynamics in energy and time. More specifically, one assumes that at any pump-probe time delay Δt, the eKE distribution consists of a weighted sum of sub-distributions, $P_i(E)$, whose individual spectral shapes do not change in time. The amount that each $P_i(E)$ contributes to the total eKE distribution at a given Δt is described by a function $T_i(\Delta t)$. The number of photoelectrons N_e with kinetic energy E within an energy interval δE is then given by

$$N_e(E, \delta E, \Delta t) = \sum_{i=A}^{D} \mathrm{T}_i(\Delta t) P_i(E) \delta E, \tag{1}$$

where $i = A, B, C$ refer to the three transient states introduced above and $i = D$ refers to the small residual signal that decays on a much longer timescale than the dynamic range of this experiment and whose energetic form, $P_D(E)$ is shown as the red curve at Δt = 3 ps in Figure 4.

Relaxation of the initially excited state A is described by a single exponential decay with time constant τ_1.

$$\mathrm{T}_A(\Delta t) = e^{-\frac{\Delta t}{\tau_1}} * \theta(\Delta t), \tag{2}$$

where $\theta(\Delta t)$ is the Heaviside step function, which is zero when the probe pulse precedes the pump and is equal to one otherwise.

The overlapping feature B is assumed to be populated on the timescale τ_1 of the decay of feature A and drained with a second time constant τ_2 according to

$$S_A \xrightarrow{\tau_1} S_B \xrightarrow{\tau_2} S_X, \tag{3}$$

where S_X represents an additional state of the system. This leads to a time-dependent signal given by

$$\mathrm{T}_B(\Delta t) = \frac{e^{-\frac{\Delta t}{\tau_2}} - e^{-\frac{\Delta t}{\tau_1}}}{1 - \frac{\tau_1}{\tau_2}} * \theta(\Delta t). \tag{4}$$

The low energy feature C has a form that we have not been able to fit to any simple kinetic models. Instead it is best reproduced as a Lorentzian in the time domain with a peak at t_C = 363(8) fs and a FWHM of Γ = 220(30) fs.

$$\mathrm{T}_C(\Delta t) = \frac{\frac{\Gamma}{2\pi}}{\left(\Delta t - t_C\right)^2 + \left(\frac{\Gamma}{2}\right)^2} * \theta(\Delta t). \tag{5}$$

At long times, a small residual signal remains as the result of channels that decay on a slow timescale compared to the dynamic range of the experiment. This is treated as a Heaviside step function.

$$\mathrm{T}_D(\Delta t) = \theta(\Delta t). \tag{6}$$

Each of these functions is then convoluted with the δt_{FWHM} = 123 fs instrument response function, which is expressed as a Gaussian:

$$g(t) = \frac{2\sqrt{\ln(2)}}{\delta t_{FWHM}\sqrt{\pi}} e^{-4\ln(2)\left(\frac{t}{\delta t_{FWHM}}\right)^2}. \tag{7}$$

Each spectral component distribution, $P_i(E)$, is divided into δE = 100 meV bins spanning the range eKE = 0.01–5.01 eV. The magnitude of each distribution integrated over each bin, $P_i(E) * \delta E$, is then treated as a floating parameter in the global fit in order to return the set of spectral functions $P_A(E)$, $P_B(E)$, and $P_C(E)$. In addition, τ_1 and τ_2 are allowed to float. The parameters Γ and t_C are fixed at the values given above, which were obtained by seperately fitting the more isolated feature C over a reduced energy range.

Figure 5(b) shows the results of a global nonlinear least squares fitting procedure compared to the data shown in Figure 5(a). The resulting three spectral components, $P_i(E)$ are shown in Figure 5(c). The intermediate feature B covers a range of energies extending both above and below that for feature A. Feature C is strongly peaked at eKE = 0 eV. Figure 5(d) shows the underlying temporal functions by which the distributions in Figure 5(c) must be multiplied in order to obtain the overall eKE distribution at a given value of Δt. The best fit values for τ_1 and τ_2 are 99(8) fs and 450(100) fs, respectively. The reported uncertainties are 1σ variations obtained by fitting multiple datasets generated by randomizing the experimental results within the error bars of the measurement. Projections of this model in the energy domain are shown as dashed lines in Figure 4.

In Figure 6, the data and model are integrated over three different energy regions to evaluate the agreement with each of the dynamical features. For reference, the relative contribution of each feature is shown for each energy range. Error bars show 3σ deviations obtained from multiple measurements. Figure 6(a) shows an integration from 1.7 to 3.2 eV, which emphasizes the contribution from feature A. In Figure 6(b), the range 3.2–4.2 eV is dominated by feature B, while in Figure 6(c) the range 0.01–0.6 eV is most strongly affected by feature C. Figure 6(d) displays all three integration regions scaled to the same maximum, emphasizing the very different dynamics associated with each feature. Overall, the good agreement between model and data for photoelectrons binned over these energy ranges provides further support for the validity of the global fit.

Note that in addition to the global fit presented above, this dataset can alternatively be analyzed by independently fitting the data integrated over different energy ranges as explained previously for the 1.6 eV probe.[26] This analysis treats the signal time dependence in the central energy region (Fig. 6(a)) as a simple exponential decay of two features, both populated within the instrument response function and decaying on timescales of τ_I = 192(10) fs and τ_{II} = 1.67(9) ps. The initial decay, τ_I, is in good agreement with the value of 220 fs obtained previously for 1.6 eV excitation using the same pump photon energies.[20] The reason for the difference between this timescale and the 99(8) fs value obtained from the global fit is apparent in Figure 6(a) where one can see that both features A and B contribute to the dynamics for electrons in this kinetic energy range. Feature B, on the other hand, can be

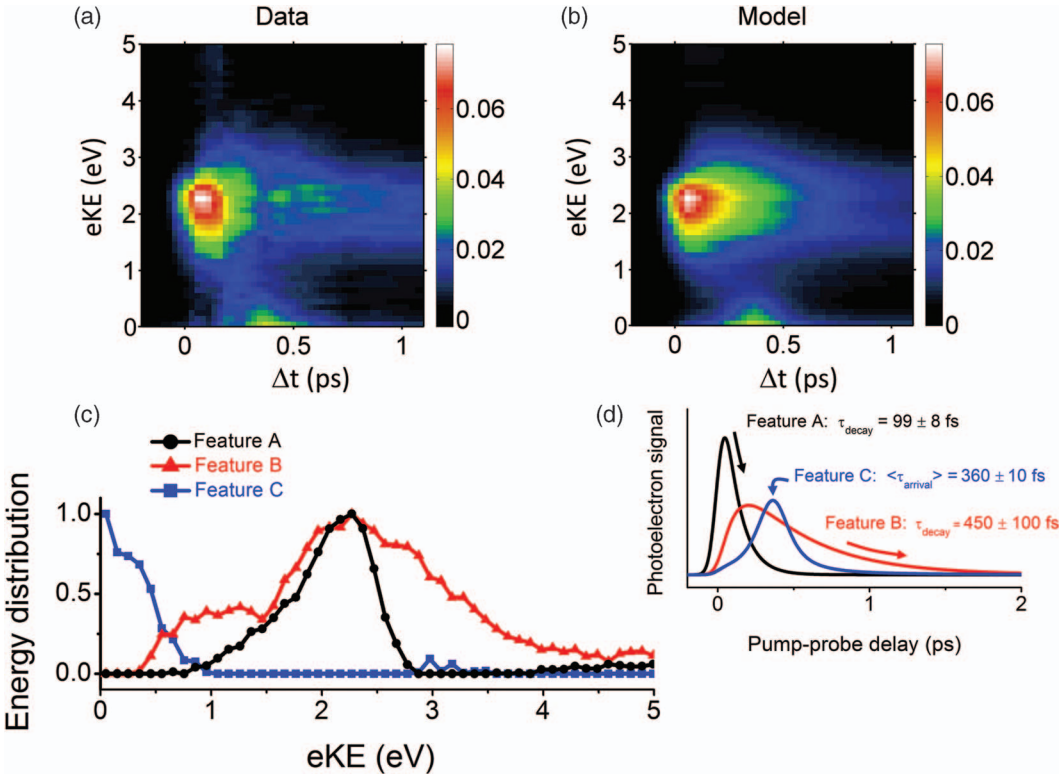

FIG. 5. Global fitting of the photoelectron kinetic energy distribution as a function of time. Dynamics are modelled as a set of three features with variable eKE spectra, each with different behavior in the time domain. The intense initially excited feature A decays on a timescale of 99(8) fs to a broader feature B which then decays within 450(100) fs. Feature C, likely associated with interband relaxation to the 1*s*2*p* band, cannot be modeled with simple kinetics and instead agrees best with a Lorentzian distribution of arrival times centered at 360 fs. (a) Photoionization spectra binned at 100 meV. (b) Best fit model. (c) Extracted spectra for all components. (d) Time dynamics of the model components. Note that the time axis in (a) and (b) shows a different range compared to Figure 3 to emphasize the dynamics of interest.

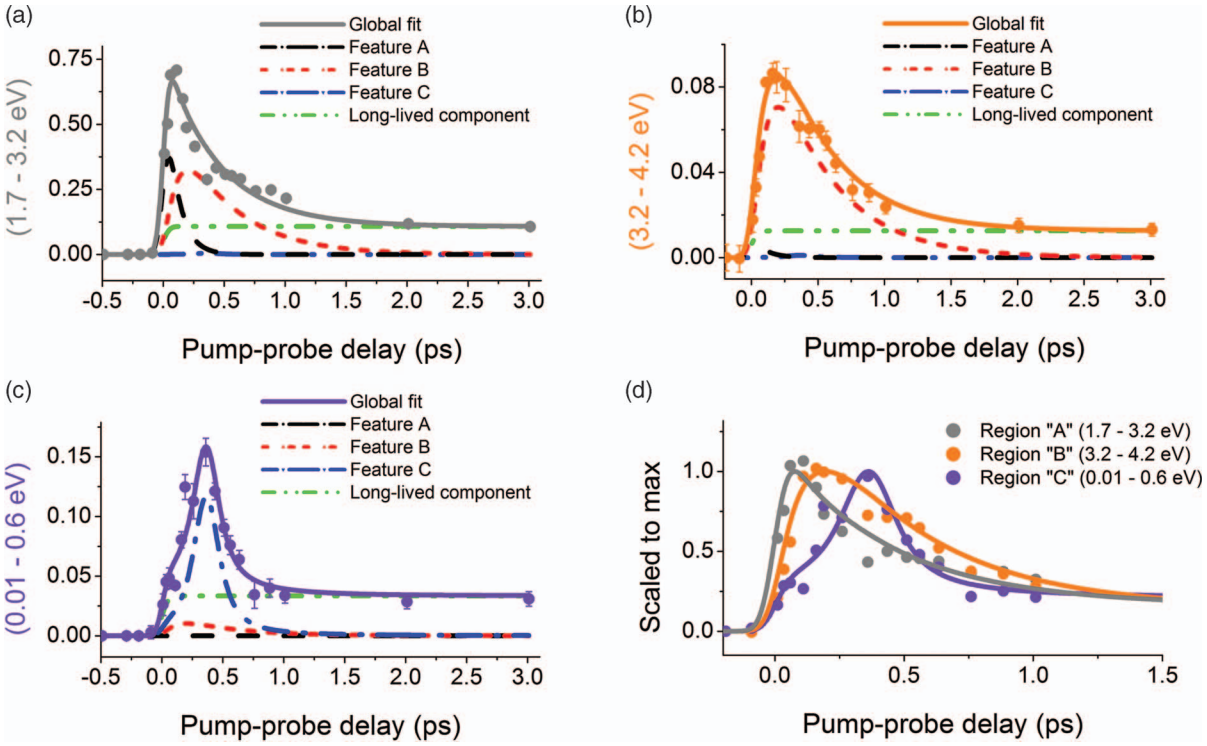

FIG. 6. Fit results from Fig. 5 integrated over several energy regions chosen to emphasize each of the three major features observed in this measurement. In each case, the contributions of all model features are shown as well as the overall fit. (a) Central energy region, covering the peaks of features A and B. (b) High-energy shoulder of the intermediate feature B. (c) Low energy region where the 1*s*2*p* feature dominates. (d) Comparison of all three energy regions scaled to the same maximum, highlighting the different dynamics observed in each case.

seen in isolation in Figure 6(b), and can be fit using Eq. (4) (with a small amplitude Heaviside step function to account for the slow-decaying channel) to return a rise time of 150(30) fs and a decay of 309(60) fs, in good agreement with the values found from the global fit.

V. DISCUSSION

This section presents a deeper examination of the three dynamical features identified here. For purposes of discussion, Figure 7 serves as a useful reference as it summarizes the relevant droplet ionization energies, band positions, and energy ranges. We then consider the origin of the surprising differences between ionization at 3.2 eV versus 1.6 eV.

A. Feature A: Ionization from the initially excited state of the system

Figure 4 shows that at $\Delta t = 10$ fs, the electron energy distribution has $eKE_{peak} = 2.3(1)$ eV, in good agreement with the value expected for vertical ionization[31] of a helium droplet,

$$h\nu_{pump}^{peak} + h\nu_{probe}^{peak} - IP_{He_N}^{vertical} = 2.4\,\text{eV}, \tag{8}$$

where $h\nu^{peak}$ refers to the most probable photon energy for each laser pulse and $IP_{He_N}^{vertical} = 24.5$ eV. This suggests, as shown in Figure 7, that feature A originates from direct ionization of droplet states that are initially excited within the $1s3p/1s4p$ band by the pump pulse and are then photoionized by the probe. With a FWHM energy span from about 23.6 eV to 24.1 eV, this band is well positioned for excitation by the pump laser, for which the FWHM photon energy distribution ranges from 23.4 to 23.9 eV.[28]

The energy distribution for feature A, extracted from the global fit and shown in Figure 5(c), represents the eKE distribution due to ionization of the initially excited state. This can be compared with the eKE distribution obtained by adding pump and probe photon energies and subtracting the droplet vertical IP. The sharp edge at high energies is a direct result of the truncation of the pump photon energy distribution by the tin filter. This further confirms that feature A represents the initially excited distribution of states in the system before relaxation has occurred. The low energy side of the photoelectron distribution, on the other hand, extends beyond what can be accounted for by the 0.5 eV uncertainty in high harmonic photon energy. This may be the result of Franck-Condon effects in direct ionization and/or electron energy loss by inelastic scattering while exiting the droplet.[20]

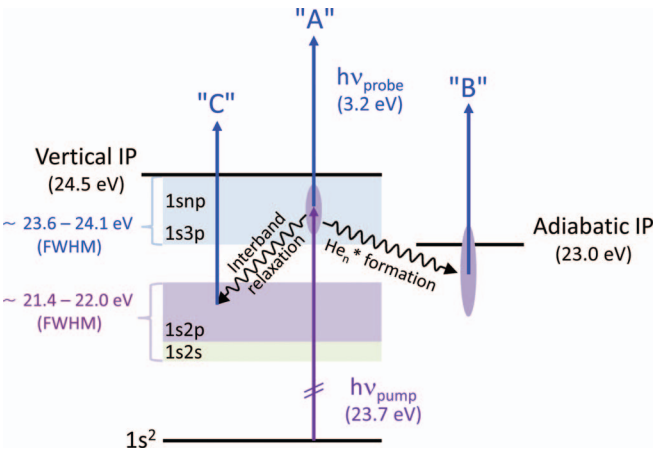

FIG. 7. Observed relaxation channels in electronically excited helium droplets. Feature A is likely due to direct ionization out of the initially excited Rydberg manifold in the $1s3p,4p$ band. Feature B grows in as feature A decays. This may be due to intraband relaxation to Rydberg core species (He_n^*) where improved Franck-Condon overlap with bound cationic clusters (He_n^+) allows spectroscopic access to the adiabatic IP. Feature C, on the other hand, is the result of, possibly collision-mediated, electronic interband relaxation.

The nature of the initially excited droplet state is of considerable interest. *Ab initio* calculations show that electronic excitation of the lower energy $1s2s$ and $1s2p$ transitions in He_{25} droplets results in states localized on single He atoms as well as more delocalized electronic wavefunctions, depending on the positions of the He atoms at the moment of excitation.[15] One may expect a similar scenario for the $1s3p/4p$ band excited in these experiments, but the extent to which the initial excitation in the much larger clusters studied here is localized on single atoms as opposed to delocalized across multiple atoms remains an open question.

B. Feature B: Cluster relaxation

As shown in Figures 3–5, feature B overlaps feature A, but is broader, weaker, and considerably longer-lived. Significantly, the high eKE range covered by feature B extends beyond the probe photon energy of 3.2 eV. These characteristics of feature B suggest that it results from intraband relaxation dynamics within the electronic state manifold initially prepared by the XUV pulse, namely the response of the He atoms to the creation of a Rydberg excitation within the droplet.[14] This excitation will lead to both attractive and repulsive interactions between neighboring helium atoms. One thus expects substantial relaxation to occur in response to electronic excitation even if the character of the initially excited state is preserved. The greater breadth of feature B most likely reflects these dynamics.

Recent calculations by Closser *et al.* provide more detailed insights into these processes.[15,16] In simulations on electronically excited He_7 a small fraction of trajectories leads to the production of bound He_2^* and He_3^*, species which have been directly observed in experiments on much larger clusters.[27] In our experiments, on droplets containing $\sim 2 \times 10^6$ atoms, we excite the higher energy $1s3p/4p$ band. Nonetheless, the calculations raise the intriguing notion that nuclear relaxation dynamics subsequent to electronic excitation can produce He_2^* and possibly larger He_n^* species within the droplet. Probe ionization of these molecular Rydberg subunits can then access strongly bound He_n^+ cations; the He_2^+ cation, for example, is bound by over 2 eV.[39] Indeed, the formation of molecular Rydberg states after electronic excitation of large droplets has been confirmed experimentally by synchroton-based fluorescence measurements in the Möller group[40] and femtosecond time-resolved ion imaging experiments in our group.[21,27]

The formation and probe-induced photoionization of these molecular Rydberg species can contribute to the

overall shape of feature B, particularly the superenergetic electrons.[17,31] The presence of He_2^* and larger He_n^* clusters within the droplet will lead to improved Franck-Condon overlap with a wider variety of droplet cation states including the cationic ground state, so that the probe pulse creates photoelectrons with higher kinetic energies than in the absence of such species. As an example, both the attractive He_2^* and He_2^+ diatomic potential energy curves have well depths up to ~2 eV, exceeding the energy difference between the atomic n = 3,4 Rydberg manifolds and the atomic Helium IP.[41–43] Moreover, while Rydberg excitations inside the droplet are generally expected to be blue-shifted with respect to the atomic limit due to the interaction between neighboring atoms, the ionic states may be blue- or red-shifted. As a result, ionic potential energy surfaces at small internuclear distances dip to energies below those of the initial Rydberg excitations. These effects, taken together, enable the release of photoelectrons with kinetic energies exceeding the probe photon energy. From another perspective, while ionization leading to feature A is largely vertical, relaxation subsequent to electronic excitation leads to more adiabatic ionization as observed in feature B. As indicated in Figure 7, this leads to higher energy photoelectrons.

In the same picture, the decay of feature B on a subpicosecond time scale is consistent with the fact that most Rydberg excitations in a droplet do not lead to stable Rydberg molecules or clusters.[27] Instead, even neighboring atoms that do approach each other after droplet excitation mostly undergo collisions that do not result in bound configurations.[16] This results in a limited time window for the production of high energy photoelectrons while two or more atoms within a Rydberg configuration are in close proximity.

We note that previous experiments using synchrotrons have detected He_2^* species ejected from the droplet subsequent to electronic excitation below the vertical IP, and autoionization of He_2^* within the droplet has been proposed as one of the mechanisms by which ZEKE electrons are produced. To the extent that these species are responsible for the electrons in feature B, this study suggests a timescale of about 100–200 fs for their formation.

C. Feature C: Interband electronic relaxation

As seen in Figures 3–6, a new feature appears and decays on a 300-400 fs timescale whose eKE distribution is peaked at 0 eV and extends to about 0.8 eV. Assuming direct ionization with the 3.2 eV probe pulse, this signal represents a band characterized by vertical binding energies $\gtrsim$ 2.4 eV. This interpretation is consistent with the fact that it was not seen in previous studies using a 1.6 eV probe pulse. The observed binding energies are likely due to ionization from the high energy side of the 1*s*2*p* droplet band, suggesting that feature C is associated with probe ionization from the same 1*s*2*p* states that could be directly accessed by a pump laser centered at $h\nu_{pump} = 21.6$ eV.

The delayed appearance of this population suggests that some time is required for the droplet to relax from the initially excited 1*s*3*p*/1*s*4*p* band to the lower lying 1*s*2*p* levels. This may be because, like feature B, the rise of feature C is closely related to nuclear motion that sets in as soon as the droplet is electronically excited. In fact, the 360 fs average relaxation time from the n = 3, 4 band to 1*s*2*p* is about four orders of magnitude shorter than the radiative lifetimes[44] of the 1*s*3*p* and 1*s*4*p* states in isolated He atoms (~2–4 ns). The rapid interband relaxation presumably occurs because at short internuclear distances, curve crossings between the n = 2 and n = 3, 4 manifolds provide routes for He + He* collisions within the droplet to efficiently transfer population from the upper to the lower droplet band.[41]

However, as shown in Figure 6(d), the dynamics of the transition 1*s*3*p*,4*p* → 1*s*2*p* are considerably more complex than the relaxation to produce feature B, as evidenced by Lorentzian shape of the 1*s*2*p* population in the time domain. The reason for this temporal behavior is not immediately apparent. It is possible that its delayed arrival could be the result of a sequential process whereby population is first transferred to state B before relaxation can occur to state C. However, the time domain dynamics seen in Figure 6(c) cannot be fit to a simple kinetic model consisting of one timescale for A to relax to B and a second for B to relax to C. Therefore, a more complicated kinetic/dynamical scheme may be at work. For this reason, the production of feature C is simply presented in Figure 7 as another relaxation channel in addition to the one responsible for feature B. As shown in Figure 6(c), feature C disappears very quickly compared to the rates of decay of features A and B. This may be due to cooling to the lower half of the 1*s*2*p* band and/or interband relaxation to the 1*s*2*s* band, all levels that are not accessible with the 3.2 eV probe photon. In fact, preliminary results from a recent free electron laser experiment support the existence of effective intra- and inter-band relaxation within the n = 2 droplet state manifold on a similar timescale.[45]

D. Comparison with results at 1.6 eV probe energy

The most notable difference between the current results probing at 3.2 eV and those at 1.6 eV is the greatly reduced fraction of anisotropic signals associated with ionization of ejected Rydberg atoms, compared to the isotropic angular distributions associated with direct ionization of electronically excited droplets.[20,26] The long-lived atomic photoelectron population, which makes up about 1/3 of the peak signal in the case of 1.6 eV probing, accounts for less than 6% of photoelectrons when using a 3.2 eV photon. Since the XUV-induced dynamics are the same in both experiments, this discrepancy points to dramatically different scaling of ionization efficiencies versus wavelength for electronically excited atomic states versus droplet states. In gas phase atoms, the excited state photoionization cross section for 1*s*3*p* decreases by a factor of 2.7 when the probe wavelength is decreased from 800 nm to 400 nm.[46] However, the persistence of the isotropic signals at 3.2 eV compared to 1.6 eV suggests that an additional effect is at play, yielding different photoionization dynamics at the two probe energies. One possible explanation is that the 1.6 eV probe is only capable of ionizing states at the droplet surface while the 3.2 eV probe provides access to the droplet interior, which contains the vast majority of atoms for the large droplets studied here. The question then is whether

one can explain enhanced bulk sensitivity for ionization at 3.2 eV vs. 1.6 eV.

Bulk liquid helium is characterized by a well-established barrier[47] of ~1.1 eV for electron injection, indicating that the conduction band in liquid He is actually above the vacuum level.[19] This barrier exists because the repulsive interaction between a free electron and neutral He forces conduction band electrons to exist in interstitial spaces within the liquid. Quantum confinement of the electrons then raises their zero point energy to 1.1 eV in reasonable agreement with simple wave mechanics calculations.[48] This repulsive force will also result in an exit barrier for an electron leaving behind a cationic core in the droplet interior. This effect has been inferred from previous experiments on Penning ionization in large ($N_{He} = 2.5 \times 10^5$) droplets[19] where photoelectron distributions were truncated at eKE < 1 eV. Such a barrier could immediately explain the differences between the current experiment and the previous results. For states below 24 eV pump excitation energy, a 3.2 eV probe photon is capable of surmounting the exit barrier but the a 1.6 eV photon is not and is therefore constrained to ionize only near the surface where such a barrier does not exist for electron emission away from the center of the droplet. Therefore, the current study may be able to observe bulk excited states, which were not accessible previously. This picture is further supported by theoretical modeling showing that the 1.6 eV results could be reproduced by considering near-surface excitations only.[20]

The interband relaxation that is directly observed in feature C was previously predicted[26] based on indirect evidence from studies using the same experimental apparatus and a 1.6 eV probe pulse. In that case, it induced a significant enhancement in ZEKE electrons,[18] a population that is present after 23.7 eV excitation and that grows larger at longer pump-probe delays when using 1.6 eV probe pulses. It was suggested that this enhancement was from probe-induced promotion of relaxed electrons from the then otherwise unobservable n = 2 bands back up to the n = 3,4 band, from which an additional fraction would be ejected in the ZEKE channel. The results presented here provide a direct confirmation that interband electronic relaxation occurs within the droplet environment. However, the new data also show that this relaxation proceeds much faster than previously suggested. Observation of ZEKE repumping in the time domain in the previous experiments yielded two separate timescales, 140–200 fs and 1.5–2.5 ps, and it was believed that the slower timescale was associated with interband relaxation.[26] In contrast, the current results clearly demonstrate that the droplet relaxes from the n = 3,4 state manifold to the n = 2 manifold within ~ 360 fs. Additionally, with the 3.2 eV probe, ZEKE regrowth only begins to appear on a timescale of ~10 ps, possibly due to the need for extensive relaxation within the n = 2 manifold before a 3.2 eV photon can resonantly promote electrons back up to the n = 3,4 states.

VI. SUMMARY/CONCLUSIONS

We have performed a femtosecond time-resolved photoelectron imaging study of pure helium nanodroplets consisting of, on average, 2×10^6 atoms each. Pumping with XUV light centered at 23.7 eV accesses the n = 3, 4 Rydberg band below the vertical droplet IP and above the adiabatic IP. Transiently populated states are probed by photoionization with 3.2 eV photons. Photoelectron VMI as a function of pump-probe delay reveals several transient electronic states in the cluster. Initially excited droplet states in the n = 3,4 Rydberg manifold are found to relax within ~ 100 fs.

Within this time interval, we observe the appearance of a strong feature that overlaps with the photoelectron distribution of the initially excited states but extends to both higher and lower electron kinetic energies. Interestingly, it extends up to 0.6 eV beyond $h\nu_{probe}$. This feature decays on a timescale of ~450 fs and is interpreted as the result of nuclear motion induced by electronic excitation within the droplet, possibly leading to the transient formation of He_n^* Rydberg cores and enhancing Franck-Condon overlap with a broad range of droplet cation geometries. As a result, the adiabatic ionization potential of the droplet becomes more relevant to the ionization dynamics, leading to higher energy photoelectrons.

A new photoelectron feature with binding energies $\gtrsim$2.4 eV, which was not accessible in previous studies, appears on a ~360 fs time scale. This result is interpreted as an electronic relaxation from the initially excited n = 3, 4 Rydberg band to the lower-lying 1*s*2*p* band. Subsequent rapid decay of this signal may be associated with continued intraband relaxation within the 1*s*2*p* band and/or interband relaxation to the 1*s*2*s* band, which is out of range of our probe energy. Rough agreement between the timescale to populate the broad feature at high kinetic energies and the delay in the appearance of 1*s*2*p* levels suggests that both features may be associated with nuclear motion. The interband relaxation, in particular, is likely the result of interatomic collisions, which provide access to crossings between the initially excited 1*s*3*p*/4*p* surface and the lower 1*s*2*p* surface.

Electron kinetic energy distributions measured with a probe photon energy of 1.6 eV are dominated by ionization of ejected Rydberg atoms. Conversely, those taken with a 3.2 eV probe are dominated by ionization of electronically excited droplets with little or no observable contribution from ejected atoms. This effect is attributed to enhanced probe ionization of bulk electronic excitations by a 3.2 eV photon, which is capable of overcoming the exit barrier associated with the above-vacuum-level conduction band edge in liquid helium.

ACKNOWLEDGMENTS

This material is based upon work supported by the U.S. Department of Energy, Office of Science, Office of Basic Energy Sciences under Contract No. DE-AC02-05CH11231. The authors would also like to thank Ming-Fu Lin, Oleg Kornilov, Darcy Peterka, and Chia Wang for helpful discussions in the course of writing this paper.

[1]S. Stringari and J. Treiner, J. Chem. Phys. **87**, 5021 (1987).
[2]S. Grebenev, J. P. Toennies, and A. F. Vilesov, Science **279**, 2083 (1998).
[3]J. P. Toennies and A. F. Vilesov, Angew. Chem., Int. Ed. Engl. **43**, 2622 (2004).
[4]S. Yang and A. M. Ellis, Chem. Soc. Rev. **42**, 472 (2013).
[5]M. Lewerenz, B. Schilling, and J. P. Toennies, J. Chem. Phys. **102**, 8191 (1995).

[6]K. Nauta and R. Miller, J. Chem. Phys. **111**, 3426 (1999).
[7]S. Grebenev *et al.*, J. Chem. Phys. **112**, 4485 (2000).
[8]E. Lugovoj, J. P. Toennies, and A. Vilesov, J. Chem. Phys. **112**, 8217 (2000).
[9]F. Stienkemeier and A. F. Vilesov, J. Chem. Phys. **115**, 10119 (2001).
[10]M. Y. Choi *et al.*, Int. Rev. Phys. Chem. **25**, 15 (2006).
[11]E. Loginov *et al.*, Phys. Rev. Lett. **106**, 233401 (2011).
[12]J. Zhang *et al.*, J. Phys. Chem. Lett. **5**, 1801 (2014).
[13]L. F. Gomez *et al.*, Science **345**, 906 (2014).
[14]K. von Haeften *et al.*, J. Phys. B: At. Mol. Opt. Phys. **38**, S373 (2005).
[15]K. D. Closser and M. Head-Gordon, J. Phys. Chem. A **114**, 8023 (2010).
[16]K. D. Closser, O. Gessner, and M. Head-Gordon, J. Chem. Phys. **140**, 134306 (2014).
[17]R. Fröchtenicht *et al.*, J. Chem. Phys. **104**, 2548 (1996).
[18]D. S. Peterka *et al.*, Phys. Rev. Lett. **91**, 043401 (2003).
[19]C. C. Wang *et al.*, J. Phys. Chem. A **112**, 9356 (2008).
[20]O. Kornilov *et al.*, J. Phys. Chem. A **115**, 7891 (2011).
[21]O. Bünermann *et al.*, IEEE J. Sel. Top. Quant. **18**, 308 (2012).
[22]D. Buchta *et al.*, J. Phys. Chem. A **117**, 4394 (2013).
[23]M. Mudrich and F. Stienkemeier, Int. Rev. Phys. Chem. **33**, 301 (2014).
[24]L. Nugent-Glandorf *et al.*, Phys. Rev. Lett. **87**, 3002 (2001).
[25]A. Stolow, A. E. Bragg, and D. M. Neumark, Chem. Rev. **104**, 1719 (2004).
[26]O. Kornilov *et al.*, J. Phys. Chem. A **114**, 6350 (2010).
[27]O. Bünermann *et al.*, J. Chem. Phys. **137**, 214302 (2012).
[28]M. Joppien, R. Karnbach, and T. Moller, Phys. Rev. Lett. **71**, 2654 (1993).
[29]M. Farnik *et al.*, Phys. Rev. Lett. **81**, 3892 (1998).
[30]D. S. Peterka, *Imaging Chemical Dynamics with the Vacuum Ultraviolet* (University of California, Berkeley, Ann Arbor, 2005), p. 183.
[31]D. S. Peterka *et al.*, J. Phys. Chem. A **111**, 7449 (2007).
[32]K. von Haeften *et al.*, J. Phys. Chem. A **115**, 7316 (2011).
[33]A. LaForge *et al.*, Sci. Rep. **4**, 3621 (2014).
[34]Y. Ovcharenko *et al.*, Phys. Rev. Lett. **112**, 073401 (2014).
[35]D. C. Morton, Q. X. Wu, and G. W. F. Drake, Can. J. Phys. **84**, 83 (2006).
[36]W. M. Haynes, *CRC Handbook of Chemistry and Physics, Internet Version*, 95 ed. (CRC Press, 2014).
[37]A. T. J. B. Eppink and D. H. Parker, Rev. Sci. Instrum. **68**, 3477 (1997).
[38]S. Ullrich *et al.*, Phys. Chem. Chem. Phys. **6**, 2796 (2004).
[39]T. L. Gilbert and A. C. Wahl, J. Chem. Phys. **55**, 5247 (1971).
[40]K. von Haeften *et al.*, Phys. Rev. Lett. **78**, 4371 (1997).
[41]S. L. Guberman and W. A. Goddard, Phys. Rev. A **12**, 1203 (1975).
[42]A. Carrington, C. H. Pyne, and P. J. Knowles, J. Chem. Phys. **102**, 5979 (1995).
[43]M. L. Ginter and R. Battino, J. Chem. Phys. **52**, 4469 (1970).
[44]G. Drake, *High Precision Calculations for Helium*, Springer Handbook of Atomic, Molecular, and Optical Physics Vol. 11 (Springer-Verlag, 2006).
[45]P. O'Keeffe *et al.*, "Relaxation dynamics of excited He nanodroplets" (unpublished).
[46]L. H. Haber, B. Doughty, and S. R. Leone, Phys. Rev. A **79**, 031401 (2009).
[47]J. R. Broomall, W. D. Johnson, and D. G. Onn, Phys. Rev. B **14**, 2819 (1976).
[48]A. F. Borghesani, *Ions and Electrons in Liquid Helium* (Oxford University Press, Oxford, 2007).